Numer. Math. (2014) 128:431–461
DOI 10.1007/s00211-014-0622-4

Numerische Mathematik

A higher order Finite Volume resolution method for a system related to the inviscid primitive equations in a complex domain

Arthur Bousquet · Gung-Min Gie · Youngjoon Hong · Jacques Laminie

Received: 14 October 2013 / Published online: 27 March 2014

Abstract We construct the cell-centered Finite Volume discretization of the two-dimensional inviscid primitive equations in a domain with topography. To compute the numerical fluxes, the so-called Upwind Scheme (US) and the Central-Upwind Scheme (CUS) are introduced. For the time discretization, we use the classical fourth order Runge–Kutta method. We verify, with our numerical simulations, that the US (or CUS) is a robust first (or second) order scheme, regardless of the shape or size of the topography and without any mesh refinement near the topography.

Mathematics Subject Classifications (1991) 65M08 · 86A10 · 76B70 · 35L65

1 Introduction

We study the two-dimensional inviscid primitive equations of the atmosphere with humidity, especially when the domain has a nonflat (mountain like) topography at the bottom. Using the linear dependency between the height and pressure of the atmosphere, we consider a version of the 2D inviscid primitive equations, where the pressure p plays the role of the negative vertical variable,

A. Bousquet · G.-M. Gie (✉) · Y. Hong
The Institute for Scientific Computing and Applied Mathematics, Indiana University,
831 East Third Street, Bloomington, IN 47405, USA
e-mail: gugie@indiana.edu

A. Bousquet
e-mail: arthbous@indiana.edu

Y. Hong
e-mail: hongy@indiana.edu

J. Laminie
Université des Antilles et de la Guyane, Fouillole, BP 250, 97157 Pointe-à-Pitre, France
e-mail: jacques.laminie@univ-ag.fr

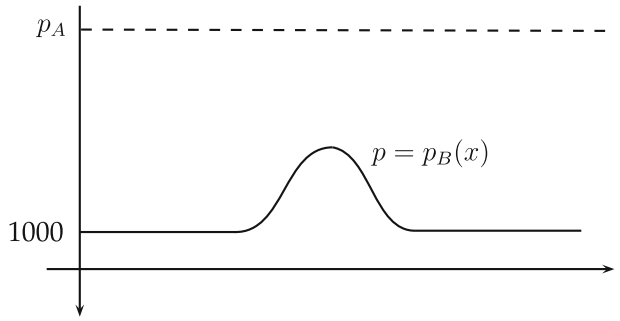

Fig. 1 Domain $\mathcal{M}$ with a topography at the *bottom*

$$\begin{cases} \dfrac{\partial T}{\partial t} + \nabla_{x,p} \cdot (uT, \omega T) - \dfrac{1}{C_p\, p}\,(R\,T - \delta\, L\, F)\,\omega = S_T & \text{in } \mathcal{M} \times (0, t_*), \\ \dfrac{\partial q}{\partial t} + \nabla_{x,p} \cdot (uq, \omega q) - \dfrac{1}{p}\,\delta\, F\, \omega = S_q & \text{in } \mathcal{M} \times (0, t_*), \\ \dfrac{\partial u}{\partial t} + \nabla_{x,p} \cdot (uu, \omega u) + \dfrac{\partial \phi}{\partial x} = S_u & \text{in } \mathcal{M} \times (0, t_*), \\ \dfrac{\partial \phi}{\partial p} + R\,\dfrac{1}{p}\,T = 0 & \text{in } \mathcal{M} \times (0, t_*), \\ \nabla_{x,p} \cdot (u, \omega) = 0 & \text{in } \mathcal{M} \times (0, t_*). \end{cases} \tag{1.1}$$

Here S_T, S_q and S_u are the smooth source functions in x, p, and t. The domain $\mathcal{M} = (0, L) \times (p_A, p_B(x))$ in $\mathbb{R}^2_{x,p}$ includes a topography at the bottom boundary described by the function $p_B(x)$ $(> p_A)$; p_B satisfies a technical assumption (see Fig. 1 and (3.3) below),

$$p_B'(x) = 0 \quad \text{near } x = 0,\ L. \tag{1.2}$$

In Fig. 1 and after, we reverse the axis in the p direction in order to reflect the physical topography (which represents a mountain).

The system (1.1) is to be solved for the velocity vector field (u, ω), the geopotential ϕ, the temperature T, and the humidity q. The other physical quantities in (1.1) are described in, e.g., [1,2], and [3] as follows:

$$\begin{cases} R = 287\ (\mathrm{JK^{-1}kg^{-1}}) \text{ is the gas constant for dry air,} \\ C_p = 1004\ (\mathrm{JK^{-1}kg^{-1}}) \text{ is the specific heat of dry air at constant pressure,} \\ L = L(T) = 2.5008 \times 10^6 - 2.3 \times 10^3\, T\ (\mathrm{Jkg^{-1}}) \text{ is the latent heat of vaporization,} \\ q_s = q_s(T, p) \text{ is the saturation specific humidity,} \\ \delta = \delta(q, \omega) = H(q - q_s)H(-\omega) \text{ where } H \text{ is the heaviside function defined by} \\ H(x) = 1/2(1 + \mathrm{sign}(x)), \\ F = F(T, p) \text{ is a given smooth function of } T \text{and } p. \end{cases} \tag{1.3}$$

The inviscid primitive equations are known to be ill-posed with any set of local type boundary conditions due to an earlier negative result in [4] or [5]. Since then, much effort has been made in theoretical and computational fluid dynamics for a better understanding of the inviscid primitive equations in a bounded domain; see, e.g., [6–13] where the authors proposed some possible (non-local) boundary conditions for the inviscid primitive equations and performed related numerical simulations. However most earlier works focused on the linearization of the inviscid primitive equations around a stratified flow, and the corresponding numerical computations were performed in a simple domain, such as a box or a channel. To date, the mathematical understanding of this topic is very scarce and remains as an important open problem. In [14] the authors considered the 2D actual primitive equations with a first order scheme. Here we consider a second order scheme with a slightly simplified physical model as explained below.

From a physical point of view, we expect that the temperature T of the atmosphere depends mainly on the height (but not on the horizontal location) in the sense that

$$T(x,\, p,\, t) \simeq \overline{T}(p,\, t), \tag{1.4}$$

where $\bar{T}(p,\, t)$ is the average temperature at the isobar p at time t. Under this physical simplifying assumption, Eq. $(1.1)_4$ implies that

$$\frac{\partial \phi}{\partial p} \simeq -\frac{R}{p}\,\overline{T},$$

and hence we see that

$$\frac{\partial \phi}{\partial x} \simeq 0 \quad \text{(see, e.g., [14]or[16]).}$$

Using this simplification, the inviscid primitive Eq. (1.1) are reduced to

$$\begin{cases} \dfrac{\partial T}{\partial t} + \nabla_{x,p} \cdot (uT, \omega T) - \dfrac{1}{C_p\, p}\,(R\,T - \delta\, L\, F)\,\omega = S_T & \text{in } \mathcal{M} \times (0, t_*), \\ \dfrac{\partial q}{\partial t} + \nabla_{x,p} \cdot (uq, \omega q) - \dfrac{1}{p}\,\delta\, F\, \omega = S_q & \text{in } \mathcal{M} \times (0, t_*), \\ \dfrac{\partial u}{\partial t} + \nabla_{x,p} \cdot (uu, \omega u) = S_u & \text{in } \mathcal{M} \times (0, t_*), \\ \nabla_{x,p} \cdot (u, \omega) = 0 & \text{in } \mathcal{M} \times (0, t_*), \end{cases} \tag{1.5}$$

where the smooth initial data is given in the form,

$$\mathbf{u}_0 = \mathbf{u}_0(x,\, p) = (T_0(p),\, q_0(x,\, p),\, u_0(x,\, p))\,. \tag{1.6}$$

The initial vertical velocity ω_0 is deduced from u_0 and the incompressibility condition as explained below.

In the simplified system (1.5), the equations of the velocity are decoupled from that of the temperature. Hence up to a certain time t_*, the system (1.5)–(1.6) is now expected to be well-posed under the physical boundary conditions which are suggested in, e.g., [14–16], or [17]:

$$\begin{cases} \dfrac{\partial T}{\partial n} = \dfrac{\partial q}{\partial n} = \dfrac{\partial u}{\partial n} = \dfrac{\partial \omega}{\partial n} = 0 & \text{at } x = 0,\ L, \\ (u,\ \omega) \cdot \boldsymbol{n} = 0 & \text{at } p = p_B, \\ \omega = 0 & \text{at } p = p_A. \end{cases} \tag{1.7}$$

Here $\boldsymbol{n}$ denotes the outer unit normal along the boundary of $\mathcal{M}$. Since the bottom boundary is described by $p = p_B(x)$, we notice that the boundary condition $(1.7)_2$ can be written in the form,

$$-u(x,\ p_B(x))\, p_B'(x) + \omega(x,\ p_B(x)) = 0, \quad 0 \le x \le L. \tag{1.8}$$

For convenience, we introduce the notation,

$$\mathbf{u} = (T,\ q,\ u), \quad \mathbf{S} = (S_T,\ S_q,\ S_u), \tag{1.9}$$

and set

$$\mathbf{F}(T, q, \omega) = (F_T,\ F_q, 0) = \left(-\frac{1}{C_p}\ (RT - \delta LF)\ \omega,\ -\delta F \omega,\ 0 \right). \tag{1.10}$$

Then the system (1.5) is written in a compact vector form,

$$\begin{cases} \frac{\partial \mathbf{u}}{\partial t} + \nabla_{x,p} \cdot (u\mathbf{u}, \omega \mathbf{u}) + \dfrac{1}{p}\, \mathbf{F} = \mathbf{S} & \text{in } \mathcal{M} \times (0, T), \\ \nabla_{x,p} \cdot (u, \omega) = 0 & \text{in } \mathcal{M} \times (0, T). \end{cases} \tag{1.11}$$

Remark 1.1 It is physically relevant to assume that the horizontal velocity u is a small perturbation of a constant speed $\overline{u}_0$ in the sense that

$$u(x,\ p,\ t) \simeq \overline{u}_0 + \widetilde{u}(x,\ p,\ t),$$

where the magnitude of $\widetilde{u}$ is much smaller than the absolute value of the constant $\overline{u}_0$. Under the assumption above, u in the system (1.5) is identical to $\widetilde{u}$ up to some lower order terms. However we do not implement this physical "simplification" in this article because the behavior of $\widetilde{u}$ is more interesting than that of u especially when the absolute value of $\overline{u}_0$ is large.

In computational fluid dynamics, Finite Volume methods (FV) are effective because of the local conservation properties of the discrete fluxes; see, e.g., [18,19]. In particular, the Central-Upwind FV methods are widely used to handle the non-linear convective terms in the study of the primitive equations (or other similar equations derived

from the conservation laws). It is so because the Central-Upwind schemes can account for the propagation of the waves at different speeds and in different directions; see, e.g., [20–26]. Concerning the domain with a non-flat boundary, one standard approach is to discretize the domain into triangular cells. However it is well-known that using the mesh with triangles is problematic to recover the normal velocity from the divergence free condition and the given tangential velocity. As an alternative, the Cartesian grid method is introduced in, e.g., [27–29]. The Cartesian grid consists mainly of rectangles, but requires some non-rectangular cells near any non-flat boundary. Hence, in this approach, the main computational errors occur near the non-flat boundary. Some additional treatment, for instance, interpolations or mesh refinements are used to overcome this issue; see also, e.g., [19]. As an other approach to treat the non-flat (or curved) boundary, one can use the transformation which maps the (curved) spatial domain to a rectangle. Yet the model equations needs to be rewritten with respect to the new variables cell by cell (see, e.g., [18]). In this article, we modify the Godunov type scheme to resolve the geometric difficulty of the system (1.5)–(1.7). Here, the discrete FV derivatives are defined by using the so-called Taylor Series Expansion Scheme (TSES) introduced in [30] and suitably modified in [31,32]. This scheme is valid for any convex quadrilateral mesh satisfying the geometric condition ($\mathcal{A}1$) below. The discrete FV derivatives on the quadrilateral mesh play an important role to recover the normal velocity from the divergence-free constraint and the given horizontal velocity; see Eqs. (3.11)–(3.13) below.

This paper is organized as follows: In Sect. 2, we recall the FV space discretization of a non-rectangular domain from [32]. Then we introduce a Runge–Kutta Finite Volume method discretization of the inviscid Eqs. (1.5)–(1.7) in Sect. 3. We present two ways to compute the numerical fluxes: The first is the Upwind Scheme (US) in Sect. 3.1 and the second is the Central-Upwind Scheme (CUS) in Sect. 3.2. For the time discretization, we use the classical fourth order Runge–Kutta method in Sect. 3.3. In Sect. 4, we investigate the flexibility of our two Finite Volume schemes towards the complex geometry. It is verified that the US and the CUS behave as a robust first and second order scheme that work well with a complex geometry by considering different shapes and sizes of the topography. It is important to observe that we do not need to introduce any mesh refinement near the topography. We believe that the US scheme and the CUS scheme introduced in this article can be made useful in many numerical studies of models derived from conservation laws.

2 Finite Volume discretization

As shown in Fig. 1, the domain $\mathcal{M} = [0, L] \times [p_A, p_B(x)]$ includes a topography at the bottom of the boundary described by the graph of $p = p_B(x)$, $0 \le x \le L$. In order to use the (cell-centered) Finite Volume method (using Taylor series expansion scheme) developed in [14,32], we first construct a partition of $\mathcal{M}$ in a set of trapezoids; see Fig. 2.

On the interval $[0, L]$ in the x direction, we choose the $N_x + 1$ uniformly distributed points $x_{i+\frac{1}{2}}$, $0 \le i \le N_x$,

$$x_{\frac{1}{2}} = 0 < x_{\frac{3}{2}} < \cdots < x_{N_x+\frac{1}{2}} = L, \tag{2.1}$$

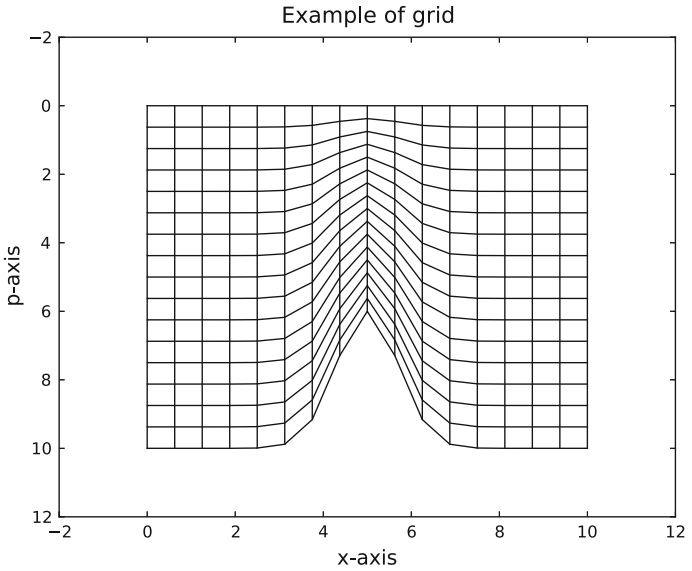

Fig. 2 Example of the spatial discretization where the topography $p_B(x)$ is given by a properly scaled normal distribution

where

$$x_{i+\frac{1}{2}} - x_{i-\frac{1}{2}} = \Delta x = \frac{L}{N_x}, \quad 1 \le i \le N_x. \tag{2.2}$$

Then for each fixed $x = x_{i+\frac{1}{2}}$, $0 \le i \le N_x$, we choose the $N_p + 1$ uniformly distributed points $p_{i+\frac{1}{2}, j+\frac{1}{2}}$, $0 \le j \le N_p$ along the interval $[p_A, p_B(x_{i+\frac{1}{2}})]$ in the p direction,

$$p_A = p_{i+\frac{1}{2}, \frac{1}{2}} < p_{i+\frac{1}{2}, \frac{3}{2}} < \cdots < p_{i+\frac{1}{2}, N_p+\frac{1}{2}} = p_B(x_{i+\frac{1}{2}}), \quad 0 \le i \le N_x, \tag{2.3}$$

where

$$p_{i+\frac{1}{2}, j+\frac{1}{2}} - p_{i+\frac{1}{2}, j-\frac{1}{2}} = \Delta p_{i+\frac{1}{2}} = \frac{p_B(x_{i+\frac{1}{2}}) - p_A}{N_p}, \quad 1 \le j \le N_p. \tag{2.4}$$

Using (2.1) and (2.3), we obtain the $(N_x + 1) \times (N_p + 1)$ nodal points in $\overline{\mathcal{M}}$,

$$\mathbf{x}_{i+\frac{1}{2}, j+\frac{1}{2}} = \left(x_{i+\frac{1}{2}},\ p_{i+\frac{1}{2}, j+\frac{1}{2}}\right), \quad 0 \le i \le N_x, \quad 0 \le j \le N_p. \tag{2.5}$$

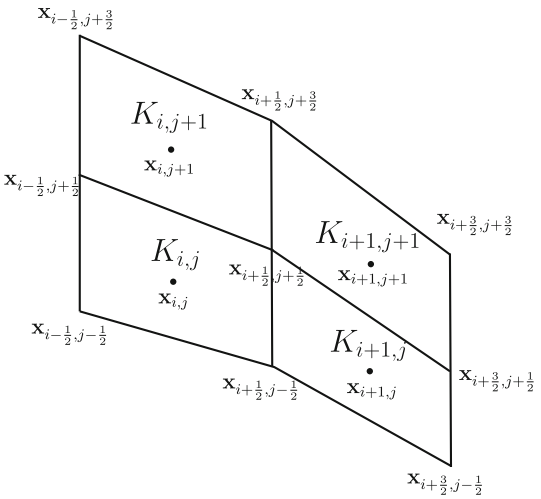

Fig. 3 A trapezoidal control volume $K_{i,j}$ with vertices $\mathbf{x}_{i\pm1/2,\, j\pm1/2}$ and the cell center $\mathbf{x}_{i,j}$, and some neighbor trapezoids

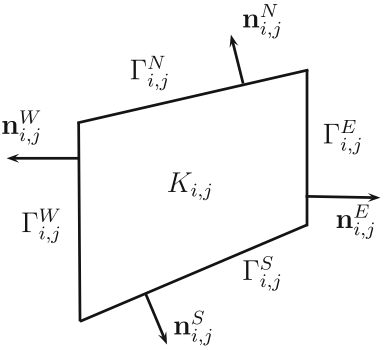

Fig. 4 Boundary $\Gamma_{i,j}$ and unit outer normal $\mathbf{n}_{i,j}$ of a control volume $K_{i,j}$

Now using the nodal points, we partition the domain $\mathcal{M}$ into $N_x \times N_p$ trapezoids $K_{i,j},\ 1 \le i \le N_x,\ 1 \le j \le N_p$ where

$$K_{i,j} := \text{trapezoidconnecting } \mathbf{x}_{i-\frac{1}{2},\,j-\frac{1}{2}},\ \mathbf{x}_{i+\frac{1}{2},\,j-\frac{1}{2}},\ \mathbf{x}_{i+\frac{1}{2},\,j+\frac{1}{2}},\ \text{and } \mathbf{x}_{i-\frac{1}{2},\,j+\frac{1}{2}}; \tag{2.6}$$

see Fig. 3.

The Finite Volume mesh defined by (2.6) is topologically equivalent to a rectangular mesh. Hence we write the boundary $\Gamma_{i,j}$ of $K_{i,j}$ as (see Fig. 4)

$$\Gamma_{i,j} = \Gamma^N_{i,j} \cup \Gamma^S_{i,j} \cup \Gamma^E_{i,j} \cup \Gamma^W_{i,j}, \quad 1 \le i \le N_x, \quad 1 \le j \le N_p. \tag{2.7}$$

Then the outer unit normal vector $\mathbf{n}_{i,j}$ of the control volume $K_{i,j}$ can be written in the form,

$$\mathbf{n}_{i,j}\big|_{\Gamma^k_{i,j}} = \mathbf{n}^k_{i,j} = (n^{k,x}_{i,j}, n^{k,p}_{i,j}), \quad k = N, S, E, W. \tag{2.8}$$

To enforce the appropriate boundary conditions, we introduce the flat control volumes along the boundary of $\mathcal{M}$:

$$\begin{cases} K_{0,j} & = \text{segment joining } \mathbf{x}_{\frac{1}{2},\, j-\frac{1}{2}} \text{ and } \mathbf{x}_{\frac{1}{2},\, j+\frac{1}{2}}, \quad 1 \le j \le N_p. \\ K_{N_x+1,j} & = \text{segment joining } \mathbf{x}_{N_x+\frac{1}{2},\, j-\frac{1}{2}} \text{ and } \mathbf{x}_{N_x+\frac{1}{2},\, j+\frac{1}{2}}, \quad 1 \le j \le N_p. \\ K_{i,0} & = \text{segment joining } \mathbf{x}_{i-\frac{1}{2},\frac{1}{2}} \text{ and } \mathbf{x}_{i+\frac{1}{2},\frac{1}{2}}, \quad 1 \le i \le N_x, \\ K_{i,N_p+1} & = \text{segment joining } \mathbf{x}_{i-\frac{1}{2},N_p+\frac{1}{2}} \text{ and } \mathbf{x}_{i+\frac{1}{2},N_p+\frac{1}{2}}, \quad 1 \le i \le N_x. \end{cases} \tag{2.9}$$

To use the convergence and consistency results for FV, which are proven in [31,32], we assume that our mesh is sufficiently regular to satisfy

($\mathcal{A}1$) The projection of $\mathbf{x}_{i,j}$ onto the line containing $\Gamma^k_{i,j}$ belongs to $\Gamma^k_{i,j}$, $k = E$, W, N, S. As a consequence of ($\mathcal{A}1$), we also have

($\mathcal{A}2$) Any nodal point $\mathbf{x}_{i+\frac{1}{2},j+\frac{1}{2}}$ in $\mathcal{M}$, $1 \le i \le N_x - 1$, $1 \le j \le N_p - 1$, is located inside the quadrilateral with vertices $\mathbf{x}_{i,j}$, $\mathbf{x}_{i,j+1}$, $\mathbf{x}_{i+1,j+1}$, and $\mathbf{x}_{i+1,j}$.

Thanks to classical geometric properties of trapezoids, the barycenter of each control volume $K_{i,j}$ can be written as an interpolation point of the four nearby vertices:

For $1 \le i \le N_x$, and $1 \le j \le N_p$, there exist $0 < \gamma^k_{i,j} < 1$, $\sum_{k=1}^4 \gamma^k_{i,j} = 1$, such that

$$\begin{aligned} \mathbf{x}_{i,j} &= (x_{i,j},\, p_{i,j}) \\ &= \gamma^1_{i,j}\, \mathbf{x}_{i-\frac{1}{2},j-\frac{1}{2}} + \gamma^2_{i,j}\, \mathbf{x}_{i+\frac{1}{2},j-\frac{1}{2}} + \gamma^3_{i,j}\, \mathbf{x}_{i+\frac{1}{2},j+\frac{1}{2}} + \gamma^4_{i,j}\, \mathbf{x}_{i-\frac{1}{2},j+\frac{1}{2}}. \end{aligned} \tag{2.10}$$

In the numerical simulations below, the explicit values of $\gamma^k_{i,j}$, $1 \le k \le 4$, are used, while here we omit the explicit expressions for the sake of simplicity.

The centers of the flat control volumes in (2.9) are denoted as follows:

$$\begin{cases} \mathbf{x}_{i,0} = \dfrac{1}{2}\left(\mathbf{x}_{i-\frac{1}{2},\frac{1}{2}} + \mathbf{x}_{i+\frac{1}{2},\frac{1}{2}}\right), \quad \mathbf{x}_{i,N_p+1} = \dfrac{1}{2}\left(\mathbf{x}_{i-\frac{1}{2},N_p+\frac{1}{2}} + \mathbf{x}_{i+\frac{1}{2},N_p+\frac{1}{2}}\right), \quad 1 \le i \le N_x, \\ \mathbf{x}_{0,j} = \dfrac{1}{2}\left(\mathbf{x}_{\frac{1}{2},j-\frac{1}{2}} + \mathbf{x}_{\frac{1}{2},j+\frac{1}{2}}\right), \quad \mathbf{x}_{N_x+1,j,j} = \dfrac{1}{2}\left(\mathbf{x}_{N_x+\frac{1}{2},j-\frac{1}{2}} + \mathbf{x}_{N_x+\frac{1}{2},j+\frac{1}{2}}\right), \quad 1 \le j \le N_p. \end{cases} \tag{2.11}$$

Now we introduce the FV space on the closure of $\mathcal{M}$:

$$V_h := \left\{ \begin{array}{l} \text{space of step functions } u_h \text{ on } \overline{\mathcal{M}} \text{ suchthat} \\ u_h|_{K_{i,j}} = u_{i,j}, \quad 0 \le i \le N_x + 1, \quad 0 \le j \le N_p + 1 \end{array} \right\}. \tag{2.12}$$

For any $u_h \in V_h$, we write

$$u_h = \sum_{i=0}^{N_x+1} \sum_{j=0}^{N_p+1} u_{i,j} \chi_{K_{i,j}}, \tag{2.13}$$

where $\chi_{K_{i,j}}$ is the characteristic function of $K_{i,j}$.

To define the FV discretized derivatives, we construct another partition of the domain $\mathcal{M}$ consisting of the quadrilaterals $K_{i,j+\frac{1}{2}}$ and $K_{i+\frac{1}{2},j}$ where

$$K_{i,j+\frac{1}{2}} := \text{quadrilateralconnecting } \mathbf{x}_{i-\frac{1}{2},j+\frac{1}{2}},\ \mathbf{x}_{i,j},\ \mathbf{x}_{i+\frac{1}{2},j+\frac{1}{2}}, \quad \text{and} \quad \mathbf{x}_{i,j+1}, \tag{2.14}$$

for $1 \le i \le N_x,\ 0 \le j \le N_p$, and

$$K_{i+\frac{1}{2},j} := \text{quadrilateralconnecting } \mathbf{x}_{i,j},\ \mathbf{x}_{i+\frac{1}{2},j-\frac{1}{2}}, \mathbf{x}_{i+1,j}, \quad \text{and} \quad \mathbf{x}_{i+\frac{1}{2},j+\frac{1}{2}}, \tag{2.15}$$

for $0 \le i \le N_x,\ 1 \le j \le N_p$.

Thanks to $(\mathcal{A}2)$, we write the inner nodal points $\mathbf{x}_{i+\frac{1}{2},j+\frac{1}{2}},\ 1 \le i \le N_x - 1,\ 1 \le j \le N_p - 1$, as a (non-unique) interpolation of the four nearby cell centers:

$$\begin{aligned}\mathbf{x}_{i+\frac{1}{2},j+\frac{1}{2}} = {} & \mu^1_{i+\frac{1}{2},j+\frac{1}{2}} \mathbf{x}_{i,j} + \mu^2_{i+\frac{1}{2},j+\frac{1}{2}} \mathbf{x}_{i+1,j} + \mu^3_{i+\frac{1}{2},j+\frac{1}{2}} \mathbf{x}_{i,j+1} \\ & + \mu^4_{i+\frac{1}{2},j+\frac{1}{2}} \mathbf{x}_{i+1,j+1},\end{aligned} \tag{2.16}$$

for some positive numbers $\mu^k_{i+\frac{1}{2},j+\frac{1}{2}}$ such that

$$\sum_{k=1}^{4} \mu^k_{i+\frac{1}{2},j+\frac{1}{2}} = 1. \tag{2.17}$$

In our numerical computations, we first fix $\mu^1_{i+\frac{1}{2},j+\frac{1}{2}}$ as a constant, e.g., $1/4$, then we solve (2.16) and (2.17) to find $\mu^k_{i+\frac{1}{2},j+\frac{1}{2}},\ k = 2, 3, 4$. Using the geometric expression (2.16), we define the approximate values of $u_h \in V_h$ at the inner nodal points:

$$\begin{aligned}u_{i+\frac{1}{2},j+\frac{1}{2}} = {} & \mu^1_{i+\frac{1}{2},j+\frac{1}{2}} u_{i,j} + \mu^2_{i+\frac{1}{2},j+\frac{1}{2}} u_{i+1,j} + \mu^3_{i+\frac{1}{2},j+\frac{1}{2}} u_{i,j+1} \\ & + \mu^4_{i+\frac{1}{2},j+\frac{1}{2}} u_{i+1,j+1},\end{aligned} \tag{2.18}$$

for $1 \le i \le N_x - 1,\ 1 \le j \le N_p - 1$.

Along the boundary, we set,

$$\begin{cases} u_{i+\frac{1}{2},\frac{1}{2}} = \dfrac{1}{2}(u_{i,0} + u_{i+1,0}), \quad u_{i+\frac{1}{2},N_p+\frac{1}{2}} = \dfrac{1}{2}(u_{i,N_p+1} + u_{i+1,N_p+1}), \quad 1 \le i \le N_x - 1, \\ u_{\frac{1}{2},j+\frac{1}{2}} = \dfrac{1}{2}(u_{0,j} + u_{0,j+1}), \quad u_{N_x+\frac{1}{2},j+\frac{1}{2}} = \dfrac{1}{2}(u_{N_x+1,j} + u_{N_x+1,j+1}), \quad 1 \le j \le N_p - 1. \end{cases} \tag{2.19}$$

At the four corners, we also set,

$$u_{\frac{1}{2},\frac{1}{2}} = u_{0,0}, \quad u_{\frac{1}{2},N_p+\frac{1}{2}} = u_{0,N_p+1}, \quad u_{N_x+\frac{1}{2},\frac{1}{2}} = u_{N_x+1,0},$$
$$u_{N_x+\frac{1}{2},N_p+\frac{1}{2}} = u_{N_x+1,N_p+1}. \tag{2.20}$$

Using the nodal values in (2.18)–(2.20), the FV derivatives on V_h, which are constant on each $K_{i+\frac{1}{2},j}$ or $K_{i,j+\frac{1}{2}}$, are defined by

$$\nabla_h u_h = \sum_{i=1}^{N_x-1}\sum_{j=1}^{N_p} \nabla_h u_h\Big|_{K_{i,j+\frac{1}{2}}} \chi_{K_{i+\frac{1}{2},j}} + \sum_{i=1}^{N_x}\sum_{j=1}^{N_p-1} \nabla_h u_h\Big|_{K_{i,j+\frac{1}{2}}} \chi_{K_{i,j+\frac{1}{2}}}, \tag{2.21}$$

where

$$\nabla_h u_h|_{K_{i+\frac{1}{2},j}} := M^{-1}_{i+\frac{1}{2},j} \begin{pmatrix} u_{i+1,j} - u_{i,j} \\ u_{i+\frac{1}{2},j+\frac{1}{2}} - u_{i+\frac{1}{2},j-\frac{1}{2}} \end{pmatrix}, \tag{2.22}$$

$$\nabla_h u_h|_{K_{i,j+\frac{1}{2}}} := M^{-1}_{i,j+\frac{1}{2}} \begin{pmatrix} u_{i+\frac{1}{2},j+\frac{1}{2}} - u_{i-\frac{1}{2},j+\frac{1}{2}} \\ u_{i,j+1} - u_{i,j} \end{pmatrix}. \tag{2.23}$$

Here $M^{-1}_{i+\frac{1}{2},j}$ and $M^{-1}_{i,j+\frac{1}{2}}$ are the inverses of the geometric matrices,

$$M_{i+\frac{1}{2},j} := \begin{pmatrix} x_{i+1,j} - x_{i,j} & p_{i+1,j} - p_{i,j} \\ 0 & p_{i+\frac{1}{2},j+\frac{1}{2}} - p_{i+\frac{1}{2},j-\frac{1}{2}} \end{pmatrix}, \tag{2.24}$$

$$M_{i,j+\frac{1}{2}} := \begin{pmatrix} x_{i+\frac{1}{2}} - x_{i-\frac{1}{2}} & p_{i+\frac{1}{2},j+\frac{1}{2}} - p_{i-\frac{1}{2},j+\frac{1}{2}} \\ x_{i,j+1} - x_{i,j} & p_{i,j+1} - p_{i,j} \end{pmatrix}. \tag{2.25}$$

The discrete L^2 (or H^1) inner product on V_h is easily inferred from (2.13) (or (2.21)):

$$(u_h, v_h)_{L^2} := \sum_{i=1}^{N_x}\sum_{j=1}^{N_p} u_{i,j} v_{i,j} |K_{i,j}|,$$

$$(u_h, v_h)_{H^1} := (u_h, v_h)_{L^2} + \sum_{i=1}^{N_x-1}\sum_{j=1}^{N_p} \left(\nabla_h u_h\big|_{K_{i+\frac{1}{2},j}} \cdot \nabla_h v_h\big|_{K_{i+\frac{1}{2},j}}\right) |K_{i+\frac{1}{2},j}|$$
$$+ \sum_{i=1}^{N_x}\sum_{j=1}^{N_p-1} \left(\nabla_h u_h\big|_{K_{i,j+\frac{1}{2}}} \cdot \nabla_h v_h\big|_{K_{i,j+\frac{1}{2}}}\right) |K_{i,j+\frac{1}{2}}|.$$

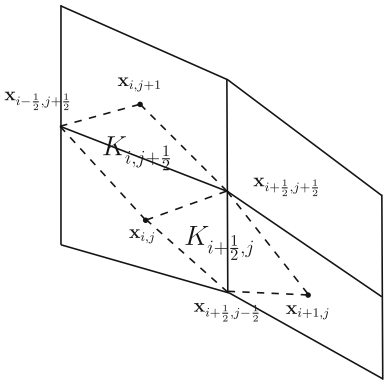

Fig. 5 Quadrilaterals $K_{i,j+\frac{1}{2}}$ and $K_{i+\frac{1}{2},j}$

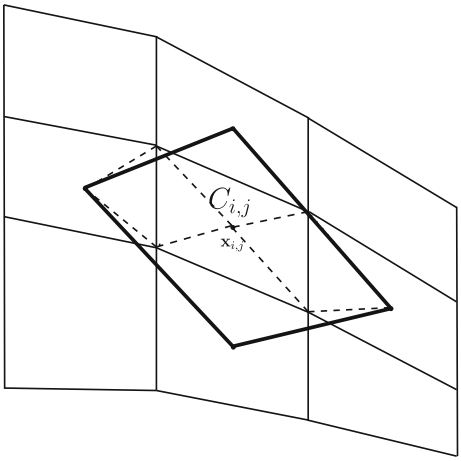

Fig. 6 A quadrilateral $C_{i,j}$ in *thick solid lines* with two nearby $K_{i\pm\frac{1}{2},j}$ in *dash-lines*

We will use the minmod function that minimize the gradient over 3 quadrilaterals to implement a second order Finite Volume method in Sect. 3.2; see (3.25) below. Toward this end, we introduce the quadrilaterals $C_{i,j}$, $1 \le i \le N_x$, $1 \le j \le N_p$, in the form,

$$C_{i,j} := \text{quadrilateralconnecting } \mathbf{x}_{i-1,j},\ \mathbf{x}_{i,j-1},\ \mathbf{x}_{i+1,j},\quad \text{and}\quad \mathbf{x}_{i,j+1};\quad (2.26)$$

see Figs. 5 and 6. In each $C_{i,j}$, we introduce a discrete derivative of $u_h \in V_h$ as

$$\nabla_h u_h|_{C_{i,j}} := M_{i,j}^{-1} \cdot \begin{pmatrix} v_{i+1,j} - v_{i-1,j} \\ v_{i,j+1} - v_{i,j-1} \end{pmatrix}, \quad (2.27)$$

where $M_{i,j}^{-1}$ is the inverse of the geometric matrix,

$$M_{i,j} := \begin{pmatrix} x_{i+1,j} - x_{i-1,j} & p_{i+1,j} - p_{i-1,j} \\ x_{i,j+1} - x_{i,j-1} & p_{i,j+1} - p_{i,j-1} \end{pmatrix}. \quad (2.28)$$

The discrete derivative (2.27) will be used in Sect. 3.2 only where we construct the Central-Upwind method.

3 Numerical scheme: the Runge–Kutta Finite Volume method

In this section, using the FV discretization from Sect. 2, we discretize the inviscid primitive Eqs. (1.5) (or (1.11)), supplemented with the initial and boundary conditions (1.6) and (1.7). We first introduce the following subspaces of V_h that reflect the boundary conditions in (1.7):

Thanks to ($\mathcal{A}2$) and the homogeneous Neumann boundary conditions on the lateral boundary of $\mathcal{M}$, we introduce the subspace $\mathcal{V}_h$ of V_h defined by

$$\mathcal{V}_h = \left\{ u_h \in V_h \,\middle|\, u_{0,j} = u_{1,j}, \quad u_{N_x+1,j} = u_{N_x,j}, \quad 0 \le j \le N_p + 1 \right\}. \tag{3.1}$$

The space $\mathcal{V}_h$ serves as the FV space for $\mathbf{u} = (T, q, u)$ in the context of the Neumann boundary conditions (1.7).

Restricting (1.8) to the FV space V_h, we write

$$\omega_{i,N_p+1} = u_{i,N_p+1}\, p_B'(x_i), \quad 0 \le i \le N_x + 1. \tag{3.2}$$

Thanks to (1.2), assuming that p_B' vanishes at x_i, $i = 1, N_x$, we notice from (3.2) that

$$\omega_{i,N_p+1} = 0, \quad i = 0, 1, N_x \text{or } N_x + 1. \tag{3.3}$$

Using (3.2) and (3.3), we project the boundary condition (1.7) of ω onto the FV space and define a subspace $\mathcal{W}_h$ of V_h as

$$\mathcal{W}_h = \left\{ \omega_h \in V_h \,\middle|\, \begin{array}{l} \omega_{0,j} = \omega_{1,j}, \quad \omega_{N_x+1,j} = \omega_{N_x,j}, \quad 0 \le j \le N_p + 1, \\ \omega_{i,0} = 0, \quad \omega_{i,N_p+1} = u_{i,N_p+1}\, p_B'(x_i), \quad 0 \le i \le N_x + 1 \end{array} \right\}. \tag{3.4}$$

To project Eq. $(1.11)_1$ of $\mathbf{u} = (T, q, u)$ onto the FV space $\mathcal{V}_h^3$, we integrate $(1.11)_1$ over a control volume $K_{i,j}$ and write

$$\frac{d\mathbf{u}_{i,j}}{dt} + \frac{1}{|K_{i,j}|} \int_{K_{i,j}} \nabla_{x,p} \cdot (u\mathbf{u}, \omega\mathbf{u}) + \frac{1}{p_{i,j}} \mathbf{F}_{i,j} = \mathbf{S}_{i,j}, \quad 1 \le i \le N_x, \quad 1 \le j \le N_p, \tag{3.5}$$

where

$$\begin{cases} \mathbf{u}_{i,j} = (T_{i,j},\, q_{i,j},\, u_{i,j}) = \dfrac{1}{|K_{i,j}|} \displaystyle\int_{K_{i,j}} \mathbf{u}, \\ \mathbf{F}_{i,j} = \mathbf{F}(T_{i,j},\, q_{i,j},\, \omega_{i,j}), \\ \mathbf{S}_{i,j} = \dfrac{1}{|K_{i,j}|} \displaystyle\int_{K_{i,j}} \mathbf{S}. \end{cases} \tag{3.6}$$

Here $|K_{i,j}|$ is the measure of $K_{i.j}$. The value $\omega_{i,j}$ of $\omega_h \in \mathcal{W}_h$ will be computed independently by using the discrete divergence-free constraint; see (3.13).

Thanks to the divergence theorem, using the outer unit normal defined in (2.8), we write the second term on the left-hand side of (3.5) in the form,

$$\frac{1}{|K_{i,j}|} \int_{K_{i,j}} \nabla_{x,p} \cdot (u\mathbf{u}, \omega\mathbf{u}) = \frac{1}{|K_{i,j}|} \left(\mathbf{H}^N_{i,j} + \mathbf{H}^S_{i,j} + \mathbf{H}^E_{i,j} + \mathbf{H}^W_{i,j} \right), \tag{3.7}$$

where

$$\begin{aligned} \mathbf{H}^N_{i,j} &= \frac{1}{|K_{i,j}|} \int_{\Gamma^N_{i,j}} \mathbf{n}^N_{i,j} \cdot \begin{pmatrix} u \\ \omega \end{pmatrix} \mathbf{u}, \qquad \mathbf{H}^S_{i,j} = \frac{1}{|K_{i,j}|} \int_{\Gamma^S_{i,j}} \mathbf{n}^S_{i,j} \cdot \begin{pmatrix} u \\ \omega \end{pmatrix} \mathbf{u}, \\ \mathbf{H}^E_{i,j} &= \frac{1}{|K_{i,j}|} \int_{\Gamma^E_{i,j}} \mathbf{n}^E_{i,j} \cdot \begin{pmatrix} u \\ \omega \end{pmatrix} \mathbf{u}, \qquad \mathbf{H}^W_{i,j} = \frac{1}{|K_{i,j}|} \int_{\Gamma^W_{i,j}} \mathbf{n}^W_{i,j} \cdot \begin{pmatrix} u \\ \omega \end{pmatrix} \mathbf{u}. \end{aligned} \tag{3.8}$$

Combining (3.5) and (3.7), we obtain the FV discretization of the system (1.5)–(1.7) which reads:

To find $\mathbf{u}_h = (T_h, q_h, u_h)$ in $(\mathcal{V}_h)^3$ such that

$$\frac{d\mathbf{u}_{i,j}}{dt} = \mathbf{R}_h(\mathbf{u}_h, \omega_h, t), \quad 1 \le i \le N_x, \quad 1 \le j \le N_p, \tag{3.9}$$

where

$$\mathbf{R}_h(\mathbf{u}_h, \omega_h, t) = -\frac{1}{|K_{i,j}|} \left(\mathbf{H}^N_{i,j} + \mathbf{H}^S_{i,j} + \mathbf{H}^E_{i,j} + \mathbf{H}^W_{i,j} \right) - \mathbf{F}_{i,j} + \mathbf{S}_{i,j}. \tag{3.10}$$

For the time discretization, we introduce, in Sect. 3.3, the fourth order Runge–Kutta scheme where the right-hand side $\mathbf{R}_h$ of (3.9) is considered as a source term at each time step. More precisely, the flux (3.8) and $-\mathbf{F}_{i,j}$ at the time step n will be computed using the given functions $\mathbf{u}_h \in \mathcal{V}_h^3$ and $\omega_h \in \mathcal{W}_h$ from the previous time step $n-1$. In Sects. 3.1 and 3.2, US scheme and CUS scheme are respectively introduced to complete the computation of the fluxes (3.8).

We find the vertical velocity ω_h from the given horizontal velocity u_h to complete the numerical computation of $(\mathbf{u}_h,\ \omega_h) \in \mathcal{V}_h^3 \times \mathcal{W}_h$ at each time step. More precisely, we restrict the incompressibility condition $(1.5)_4$ to $\cup_{i=1}^{N_x} \cup_{j=0}^{N_p} K_{i,j+1/2}$ only, and write

$$\nabla_h \omega_h \cdot (0,1)\big|_{K_{i,j+\frac{1}{2}}} = -\nabla_h u_h \cdot (1,0)\big|_{K_{i,j+\frac{1}{2}}}, \quad 1 \le i \le N_x, \quad 0 \le j \le N_p. \tag{3.11}$$

Thanks to the construction of our Finite Volume mesh in Sect. 2, we notice that the vector $\mathbf{x}_{i,j} - \mathbf{x}_{i,j+1}$ for each i, j is almost parallel to the p-direction. Hence, using the Finite Volume derivative defined in (2.23), we write (3.11) in the form,

$$\begin{aligned} \omega_{i,j+1} - \omega_{i,j} &= -(p_{i,j+1} - p_{i,j}) \left(\nabla_h u_h \cdot (1,0)\big|_{K_{i,j+\frac{1}{2}}} \right), \\ & 1 \le i \le N_x, \quad 1 \le j \le N_p, \end{aligned} \tag{3.12}$$

with $\omega_{i,0} = 0$ because $\omega_h \in \mathcal{W}_h$. We rewrite (3.12) in a matrix form

$$\mathcal{A}_h \omega_h = \mathcal{F}_h(u_h), \tag{3.13}$$

where $F_h(u_h)$ is the right-hand side and $\mathcal{A}_h \omega_h$ is the left-hand side of (3.12). Since we have $\omega_{i,0} = 0$, for $1 \le i \le N_x$, Eq. (3.13) has a unique solution $\omega \in \mathcal{W}_h$ for a given $u_h \in \mathcal{V}_h$.

Remark 3.1 The values of $\mathbf{u}_h \in (\mathcal{V}_h)^3$ at the top and bottom boundaries remain undetermined. We only need these free values of $\mathbf{u}_h$ for the computation of the fluxes at the top and the bottom boundaries. Yet these free values of $\mathbf{u}_h$ are multiplied by $(u_h,\ \omega_h) \cdot \boldsymbol{n}$, see Eq. (3.8).

Since $(u_h,\ \omega_h) \cdot \boldsymbol{n} = 0$ at the top and the bottom boundaries (see (3.4)), we can simply take the free values $\mathbf{u}_h$ equal to zero in the computation.

3.1 Upwind Scheme (US)

In this section, we present the US scheme, which is used to approximate the fluxes in (3.8). The following US construction, in this section, resembles those of earlier works in [14].

It is necessary to introduce some interpolated values of $u_h \in \mathcal{V}_h$ and $\omega_h \in \mathcal{W}_h$ at the center of each edge in order to compute the fluxes via US. Using the fact that the barycenters are well-aligned in the p-direction, the interpolation value on the north and south edges of u_h (or ω_h) are simply defined by

$$\begin{cases} u_{i,\frac{1}{2}} = u_{i,0} \quad \omega_{i,\frac{1}{2}} = \omega_{i,0} \quad 1 \le i \le N_x, \\ u_{i,j+\frac{1}{2}} = \dfrac{u_{i,j} + u_{i,j+1}}{2}, \quad \omega_{i,j+\frac{1}{2}} = \dfrac{\omega_{i,j} + \omega_{i,j+1}}{2} \quad 1 \le i \le N_x, \quad 1 \le j \le N_p, \\ u_{i,N_p+\frac{1}{2}} = u_{i,N_p+1} \quad \omega_{i,N_p+\frac{1}{2}} = \omega_{i,N_p+1} \quad 1 \le i \le N_x. \end{cases} \tag{3.14}$$

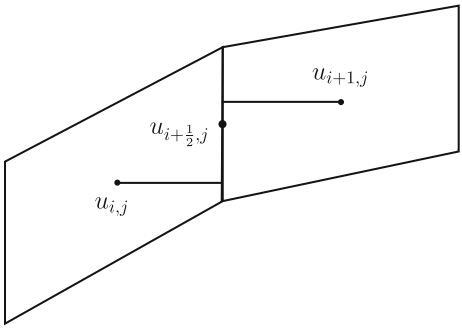

Fig. 7 The central value $u_{i+\frac{1}{2},j}$ along a vertical edge as a interpolation of two projections of $u_{i,j}$ and $u_{i+1,j}$ along the edge

Then applying the US scheme to (3.14), the north and south fluxes in (3.8) are as follows:

$$\mathbf{H}^N_{i,j} \simeq \frac{|\Gamma^N_{i,j}|}{|K_{i,j}|}\mathbf{n}^N_{i,j} \cdot \begin{pmatrix} u_{i,j+\frac{1}{2}} \\ \omega_{i,j+\frac{1}{2}} \end{pmatrix} \check{\mathbf{u}}_{i,j+\frac{1}{2}}, \tag{3.15}$$

$$\mathbf{H}^S_{i,j} \simeq \frac{|\Gamma^S_{i,j}|}{|K_{i,j}|}\mathbf{n}^S_{i,j} \cdot \begin{pmatrix} u_{i,j-\frac{1}{2}} \\ \omega_{i,j-\frac{1}{2}} \end{pmatrix} \check{\mathbf{u}}_{i,j-\frac{1}{2}}, \tag{3.16}$$

where $|\Gamma^N_{i,j}|$ and $|\Gamma^S_{i,j}|$ are the lengths of the segments $\Gamma^N_{i,j}$ and $\Gamma^S_{i,j}$. Then for $1 \le i \le N_x$ and $1 \le j \le N_p$, we define

$$\check{\mathbf{u}}_{i,j+\frac{1}{2}} = \begin{cases} \mathbf{u}_{i,j} & \text{if } \mathbf{n}^N_{i,j} \cdot \begin{pmatrix} u_{i,j+\frac{1}{2}} \\ \omega_{i,j+\frac{1}{2}} \end{pmatrix} \ge 0, \\ \mathbf{u}_{i,j+1} & \text{if } \mathbf{n}^N_{i,j} \cdot \begin{pmatrix} u_{i,j+\frac{1}{2}} \\ \omega_{i,j+\frac{1}{2}} \end{pmatrix} < 0. \end{cases} \tag{3.17}$$

Note that, in (3.15) (or (3.16)), it is not necessary to choose $\check{\mathbf{u}}_{i,N_p+\frac{1}{2}}$ (or $\check{\mathbf{u}}_{i,\frac{1}{2}}$) because $(u_{i,N_p+1},\ \omega_{i,N_p+1})\cdot \boldsymbol{n}^N_{i,N_p} = 0$ (or $(u_{i,0},\ \omega_{i,0})\cdot \boldsymbol{n}^S_{i,1} = 0$). This is due to the construction of the FV spaces $\mathcal{V}_h$ and $\mathcal{W}_h$ defined in (3.1) and (3.4); see Remark 3.1.

To compute the east and west fluxes in (3.8), we introduce an interpolation value on the east (or west) edge of u_h in the form,

$$u_{i+\frac{1}{2},j} = r u_{i,j+1} + (1-r)u_{i,j}, \quad 0 \le i \le N_x, \quad 1 \le j \le N_p. \tag{3.18}$$

Here $r = (p_{i+\frac{1}{2},j} - p_{i,j})/(p_{i+1,j} - p_{i,j})$ is a geometric value, which is determined by the projection of the barycenter onto the east (or west) edge; see Fig. 7.

Note that we do not need to introduce any interpolation of ω on the east and west edges because the outer normal vectors on those edges are orthogonal to the

p-direction. We compute the east and west fluxes in (3.8) by applying the US scheme to (3.18) and setting

$$\mathbf{H}^E_{i,j} \simeq \frac{|\Gamma^E_{i,j}|}{|K_{i,j}|} u_{i+\frac{1}{2},j} \check{\mathbf{u}}_{i+\frac{1}{2},j}, \tag{3.19}$$

$$\mathbf{H}^W_{i,j} \simeq -\frac{|\Gamma^W_{i,j}|}{|K_{i,j}|} u_{i+\frac{1}{2},j} \check{\mathbf{u}}_{i-\frac{1}{2},j}, \tag{3.20}$$

where $|\Gamma^E_{i,j}|$ and $|\Gamma^W_{i,j}|$ are the lengths of the segments $\Gamma^E_{i,j}$, $\Gamma^W_{i,j}$, and for $0 \le i \le N_x$ and $1 \le j \le N_p$,

$$\check{\mathbf{u}}_{i+\frac{1}{2},j} = \begin{cases} \mathbf{u}_{i,j} & \text{if } u_{i+\frac{1}{2},j} \ge 0, \\ \mathbf{u}_{i,j+1} & \text{if } u_{i+\frac{1}{2},j} < 0. \end{cases} \tag{3.21}$$

Then we obtain the US scheme for Eq. (3.8) from Eqs. (3.15), (3.16), (3.19) and (3.20).

3.2 Central-Upwind Scheme (CUS)

In this section, modifying the 2nd order central-upwind method as in e.g., [20–26], we construct a higher order CUS to compute the flux appearing in (3.8). As it will be experimentally verified by the numerical computations below in Sect. 4, this CUS scheme gives a better convergence rate, of order about 1.5 with respect to the mesh size, than that of order 1 for the US scheme introduced in the previous section.

The fluxes in (3.8) can be estimated by the CUS scheme in the form,

$$\mathbf{H}^k_{i,j} \simeq \frac{|\Gamma^k_{i,j}|}{|K_{i,j}|} \left(\mathbf{h}^k_{i,j} \cdot \mathbf{n}^k_{i,j} \right), \quad \mathbf{h}^k_{i,j} = (\mathbf{h}^{k,x}_{i,j}, \mathbf{h}^{k,p}_{i,j}), \tag{3.22}$$

for $k = N, E, W, S$, $1 \le i \le N_x$ and $1 \le j \le N_p$, where $\mathbf{h}^k_{i,j}$ will be determined below. Along each east or west edges, since the unit outer normal is parallel to the x-direction, we do not need to introduce $\mathbf{h}^{k,p}$, $k = E, W$ in (3.22). Moreover, since the south (or west) flux of one control volume can be understood as the negative north (or east) flux of a nearby control volume, we have $\mathbf{H}^S_{i,j} = -\mathbf{H}^N_{i,j-1}$ and $\mathbf{H}^W_{i,j} = -\mathbf{H}^E_{i-1,j}$ for each i, j. Therefore, to complete the formula (3.22), it is enough to define $\mathbf{h}^{N,x}_{i,j}$, $\mathbf{h}^{N,p}_{i,j}$, and $\mathbf{h}^{E,x}_{i,j}$ for $1 \le i \le N_x$ and $1 \le j \le N_p$ below:

We introduce $\mathbf{u}^{N+}_{i,j} = (T^{N+}_{i,j}, q^{N+}_{i,j}, u^{N+}_{i,j})$ (or $\mathbf{u}^{N-}_{i,j} = (T^{N-}_{i,j}, q^{N-}_{i,j}, u^{N-}_{i,j})$) as an approximation of $\mathbf{u}_h$ near $\Gamma^N_{i,j}$ of $K_{i,j}$ from above (or below) of $\Gamma^N_{i,j}$. Similarly, $\mathbf{u}^{E+}_{i,j} = (T^{E+}_{i,j}, q^{E+}_{i,j}, u^{E+}_{i,j})$ (or $\mathbf{u}^{E-}_{i,j} = (T^{E-}_{i,j}, q^{E-}_{i,j}, u^{E-}_{i,j})$) denotes an approximation of $\mathbf{u}_h$ near $\Gamma^E_{i,j}$ of $K_{i,j}$ from the right (or left) of $\Gamma^N_{i,j}$. These approximations $\mathbf{u}^{k\pm}_{i,j}$, $k = N, E$, $1 \le i \le N_x$ and $1 \le j \le N_p$, are defined by a non-oscillatory linear

polynomial reconstruction

$$\begin{aligned}\mathbf{u}_{i,j}^{N-} &:= \boldsymbol{\zeta}_{i,j}^{N}(x_{i,j+\frac{1}{2}}, p_{i,j+\frac{1}{2}}, t), \quad \mathbf{u}_{i,j}^{N+} := \boldsymbol{\zeta}_{i,j+1}^{N}(x_{i,j+\frac{1}{2}}, p_{i,j+\frac{1}{2}}, t),\\ \mathbf{u}_{i,j}^{E-} &:= \boldsymbol{\zeta}_{i,j}^{E}(x_{i+\frac{1}{2},j}, p_{i+\frac{1}{2},j}, t), \quad \mathbf{u}_{i,j}^{E+} := \boldsymbol{\zeta}_{i+1,j}^{E}(x_{i+\frac{1}{2},j}, p_{i+\frac{1}{2},j}, t),\end{aligned} \tag{3.23}$$

where

$$\begin{cases}\boldsymbol{\zeta}_{i,j}^{N}(\bar{x}, \bar{p}, t) := \mathbf{u}_{i,j}(t) + \mathbf{s}_{i,j}^{N}(\bar{x}, \bar{p}, t),\\ \boldsymbol{\zeta}_{i,j}^{E}(\bar{x}, \bar{p}, t) := \mathbf{u}_{i,j}(t) + \mathbf{s}_{i,j}^{E}(\bar{x}, \bar{p}, t).\end{cases} \tag{3.24}$$

Here using the Finite Volume derivatives in (2.21) and (2.27), the slopes $\mathbf{s}_{i,j}^{N}$ and $\mathbf{s}_{i,j}^{E}$ are defined by

$$\begin{aligned}&\mathbf{s}_{i,j}^{N}(\bar{x}, \bar{p}, t)\\ &\quad = \text{minmod}\left(\boldsymbol{\theta}_1 \otimes \frac{\mathbf{u}_{i,j} - \mathbf{u}_{i,j-1}}{\Delta\tilde{p}_i},\ \frac{\mathbf{u}_{i,j+1} - \mathbf{u}_{i,j-1}}{2\Delta\tilde{p}_i},\ \boldsymbol{\theta}_1 \otimes \frac{\mathbf{u}_{i,j+1} - \mathbf{u}_{i,j}}{\Delta\tilde{p}_i}\right)(p_{i,j} - \overline{p}),\\ &\mathbf{s}_{i,j}^{E}(\bar{x}, \bar{p}, t)\\ &\quad = \text{minmod}\left(\boldsymbol{\theta}_1 \otimes \left(\nabla\mathbf{u}_h|_{K_{i-\frac{1}{2},j}} \cdot \mathbf{x}\right),\ \nabla\mathbf{u}_h|_{C_{i,j}} \cdot \mathbf{x},\ \boldsymbol{\theta}_1 \otimes \left(\nabla\mathbf{u}_h|_{K_{i+\frac{1}{2},j}} \cdot \mathbf{x}\right)\right),\end{aligned} \tag{3.25}$$

for $\Delta\tilde{p}_i = (\Delta p_{i+1/2} + \Delta p_{i-1/2})/2$, $\mathbf{x} = (x_{i,j} - \bar{x},\ p_{i,j} - \bar{p})$, and $\boldsymbol{\theta}_i = (\theta_i^1, \theta_i^2, \theta_i^3)$, $i = 1, 2$. In (3.25), the operator $\otimes$ acts on two vectors and produce a vector whose n-th component is the product of n-th components of the input vectors. The minmod limiter in (3.25) is defined by

$$\text{minmod}\ (x_1, x_2, ..) := \begin{cases}\min(x_i), & \text{if } x_i > 0 \quad \forall i,\\ \max(x_i), & \text{if } x_i < 0 \quad \forall i,\\ 0, & \text{otherwise.}\end{cases}$$

Moreover, we choose the parameters $\theta_i^j \in [1, 2]$, $i = 1, 2$, $j = 1, 2, 3$ in an empirical way.

Let us denote

$$\mathbf{v}_h = (\mathbf{u}_h, \omega_h), \tag{3.26}$$

then $\mathbf{v}_{i,j}^{k\pm} = (\mathbf{u}_{i,j}^{k\pm}, \omega_{i,j}^{k\pm})$, $k = N, E$, $1 \le i \le N_x$ and $1 \le j \le N_p$, are defined in the same manner as $\mathbf{u}_h$.

We set

$$\begin{aligned}a_{i,j}^{N+} &= \max\left[u_{i,j}^{N+}, u_{i,j}^{N-}, 0\right], \quad a_{i,j}^{N-} = \min\left[u_{i,j}^{N+}, u_{i,j}^{N-}, 0\right],\\ a_{i,j}^{E+} &= \max\left[u_{i,j}^{E+}, u_{i,j}^{E-}, 0\right], \quad a_{i,j}^{E-} = \min\left[u_{i,j}^{E+}, u_{i,j}^{E-}, 0\right],\\ b_{i,j}^{N+} &= \max\left[\omega_{i,j}^{N+}, \omega_{i,j}^{N-}, 0\right], \quad b_{i,j}^{N-} = \min\left[\omega_{i,j}^{N+}, \omega_{i,j}^{N-}, 0\right].\end{aligned} \tag{3.27}$$

Then we finally define

$$\mathbf{h}_{i,j}^{N,x} = \frac{a_{i,j}^{N+} F(\mathbf{u}_{i,j}^{N-}) - a_{i,j}^{N-} F(\mathbf{u}_{i,j}^{N+})}{a_{i,j}^{N+} - a_{i,j}^{N-}} + \frac{a_{i,j}^{N+} a_{i,j}^{N-} (\mathbf{u}_{i,j}^{N+} - \mathbf{u}_{i,j}^{N-})}{a_{i,j}^{N+} - a_{i,j}^{N-}}, \tag{3.28}$$

$$\mathbf{h}_{i,j}^{N,p} = \frac{b_{i,j}^{N+} G(\mathbf{v}_{i,j}^{N-}) - b_{i,j}^{N-} G(\mathbf{v}_{i,j}^{N+})}{b_{i,j}^{N+} - b_{i,j}^{N-}} + \frac{b_{i,j}^{N+} b_{i,j}^{N-} (\mathbf{v}_{i,j}^{N+} - \mathbf{v}_{i,j}^{N-})}{b_{i,j}^{N+} - b_{i,j}^{N-}}, \tag{3.29}$$

$$\mathbf{h}_{i,j}^{E,x} = \frac{a_{i,j}^{E+} F(\mathbf{u}_{i,j}^{E-}) - a_{i,j}^{E-} F(\mathbf{u}_{i,j}^{E+})}{a_{i,j}^{E+} - a_{i,j}^{E-}} + \frac{a_{i,j}^{E+} a_{i,j}^{E-} (\mathbf{u}_{i,j}^{E+} - \mathbf{u}_{i,j}^{E-})}{a_{i,j}^{E+} - a_{i,j}^{E-}}, \tag{3.30}$$

where $F(\mathbf{u}) = (uT,\ uq,\ u^2)$ and $G(\mathbf{v}) = (\omega T,\ \omega q,\ \omega u)$. This construction of $\mathbf{h}_{i,j}^{N,p}$, $\mathbf{h}_{i,j}^{N,p}$, and $\mathbf{h}_{i,j}^{E,x}$ completes the computation of the fluxes in (3.22).

3.3 Fourth order Runge–Kutta time discretization

For the time discretization, we introduce, in this section, the classical fourth order Runge–Kutta method.

For a fixed time $t_* > 0$, we set $\Delta t = t_*/N_t$ as the uniform time increment where N_t denotes the total number of iterations.

The initial value $(\mathbf{u}_h^0, \omega_h^0)$ where $\mathbf{u}_h^0 = (T_h^0, q_h^0, u_h^0)$ is defined as the projection of the initial data $(\mathbf{u}_0, \omega_0)$ in (1.6) onto the space $(\mathcal{V}_h)^3 \times \mathcal{W}_h$. Then, thanks to (3.9) and (3.13), we obtain the time discrete solution $(\mathbf{u}_h^n, \omega_h^n)$, $\mathbf{u}_h^n = (T_h^n, q_h^n, u_h^n)$ at time step $1 \le n \le N_t$ by recursively applying the process below:

Step 1

$$\begin{aligned} \mathbf{k}^{1,n} &= \mathbf{R}_h(\mathbf{u}_h^n, \omega_h^n, t_n), \\ \mathbf{u}_h^{1,n} &= \mathbf{u}_h^n + \Delta t\, \mathbf{k}^{1,n}, \\ \mathcal{A}_h \omega_h^{1,n} &= \mathcal{F}_h(u_h^{1,n}), \end{aligned} \tag{3.31}$$

Step 2

$$\begin{aligned} \mathbf{k}^{2,n} &= \mathbf{R}_h(\mathbf{u}_h^{1,n}, \omega_h^{1,n}, t_n + \frac{\Delta t}{2}), \\ \mathbf{u}_h^{2,n} &= \mathbf{u}_h^n + \frac{\Delta t}{2}\, \mathbf{k}^{2,n}, \\ \mathcal{A}_h \omega_h^{2,n} &= \mathcal{F}_h(u_h^{2,n}), \end{aligned} \tag{3.32}$$

Step 3

$$\begin{aligned} \mathbf{k}^{3,n} &= \mathbf{R}_h(\mathbf{u}_h^{2,n}, \omega_h^{2,n}, t_n + \frac{\Delta t}{2}), \\ \mathbf{u}_h^{3,n} &= \mathbf{u}_h^n + \frac{\Delta t}{2}\, \mathbf{k}^{3,n}, \\ \mathcal{A}_h \omega_h^{3,n} &= \mathcal{F}_h(u_h^{3,n}), \end{aligned} \tag{3.33}$$

Step 4

$$\begin{aligned}\mathbf{k}_4^n &= \mathbf{R}_h(\mathbf{u}_h^{3,n}, \omega_h^{3,n}, t_n + \Delta t),\\ \mathbf{u}_h^{n+1} &= \mathbf{u}_h^n + \frac{\Delta t}{6}\left(\mathbf{k}^{1,n} + 2\mathbf{k}^{2,n} + 2\mathbf{k}^{3,n} + \mathbf{k}_4^n\right),\\ \mathcal{A}_h\omega_h^{n+1} &= \mathcal{F}_h(u_h^{n+1}).\end{aligned} \tag{3.34}$$

4 Numerical simulations

We report, in this section, the results of some numerical tests for the inviscid primitive Eqs. (1.5)–(1.7) performed by using the Runge–Kutta Finite Volume method constructed in Sect. 3. The domain $\mathcal{M}$ includes a topography (regarded as a mountain) which is described by a smooth function $p_B(x)$; see Fig. 1. For the physical relevance of our simulations, the length of the domain in the x-direction L and the minimum pressure p_A are chosen respectively as $L = 50{,}000$ and $p_A = 200$, and we set the final time $t_* = 500$ and the time step $\Delta t = 10$. Then, the exact solution of (1.5) is chosen as

$$\begin{cases} T_{EX}(p,t) = \left(300 - 50\left(1 - \frac{p}{1000}\right)\right)\cos(2\pi t),\\ q_{EX}(x,p,t) = \left(\frac{p-p_B(x))}{1200.0}\right)^2 \cos\left(\frac{4\pi p}{p_B(x)}\right)\cos(4\pi t) + 0.4,\\ u_{EX}(x,p,t) = -\frac{\partial \xi}{\partial p},\\ w_{EX}(x,p,t) = \frac{\partial \xi}{\partial x}, \end{cases} \tag{4.1}$$

where

$$\xi(x,p,t) = \left(\frac{(p-p_A)(p_B(x)-p)^2}{50\times 1000^2}\right)^3 \cos(2\pi t). \tag{4.2}$$

Now, our main task is to perform the numerical simulations of the inviscid primitive equations by applying the US and the CUS discretizations. By changing the size and shape of the topography, we aim to verify that the US and the CUS are convergent FV schemes of order 1 and order around 1.5 respectively with respect to the spatial mesh. Towards this end, we first test the US scheme and the CUS scheme with a relatively small topography in Sect. 4.1. Concerning the US scheme for this case, we see that the convergence rate of q or u is of order one as desired. By our treatment of the incompressibility condition, which reflects the geometry very well (see (3.11)), the convergence rate of the vertical velocity ω is of order 2. We believe that the method (3.11)–(3.13), introduced in this article, can be made useful in many numerical computations of incompressible fluids in particular when the domain has a non-flat boundary. Due to the choice of T as a physical data independent of x (see (1.4) and $(4.1)_1$), the convergence rate of T is as low as of order 0.1. However the relative L^2 error of T is still small as it stays between 10^{-4} and 10^{-5}. Once we perform the simulation using CUS scheme on the relatively flat topography, we notice that the convergence rates of the CUS are about $1.3 \sim 1.6$ times better than those of the US. Hence we believe that the CUS can be considered as a second order scheme in general; see Remark 4.1 below. To test the flexibility of our FV schemes towards the geometry, we consider the cases of a high topography in Sect. 4.2 and a narrow mountain in Sect. 4.3. For these cases, we notice that the US (or the CUS) scheme produces almost the same convergence results as that of the relatively flat topography. Therefore, we finally claim that our US (or CUS) scheme is a robust first (or second) order scheme which works well with a relatively complex geometry.

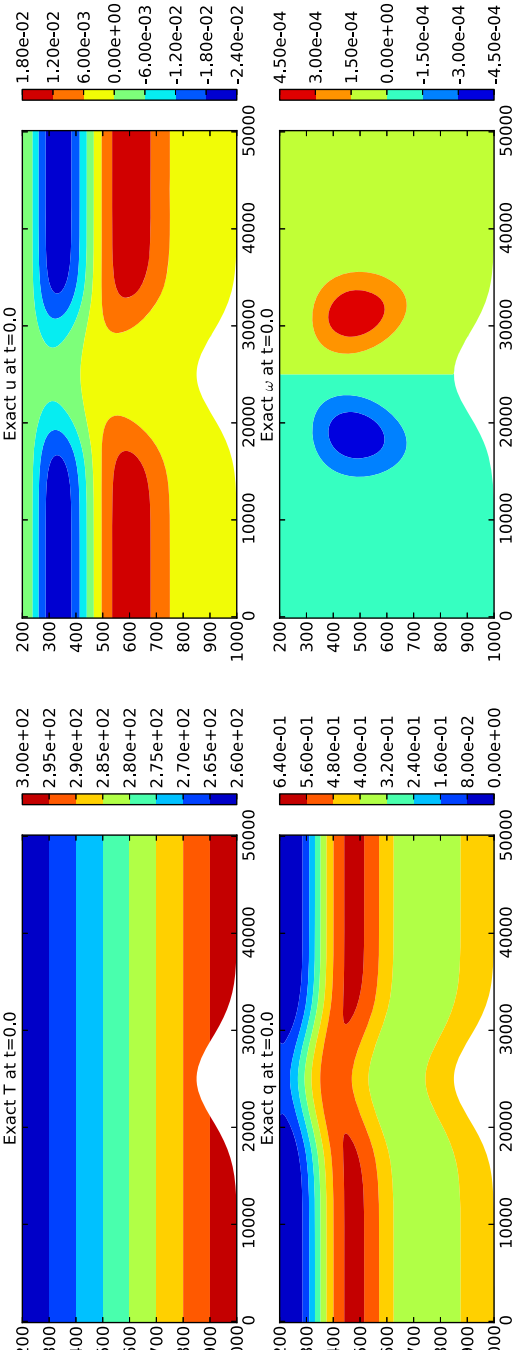

Fig. 8 Initial values of T, q, u, and ω with (4.3)

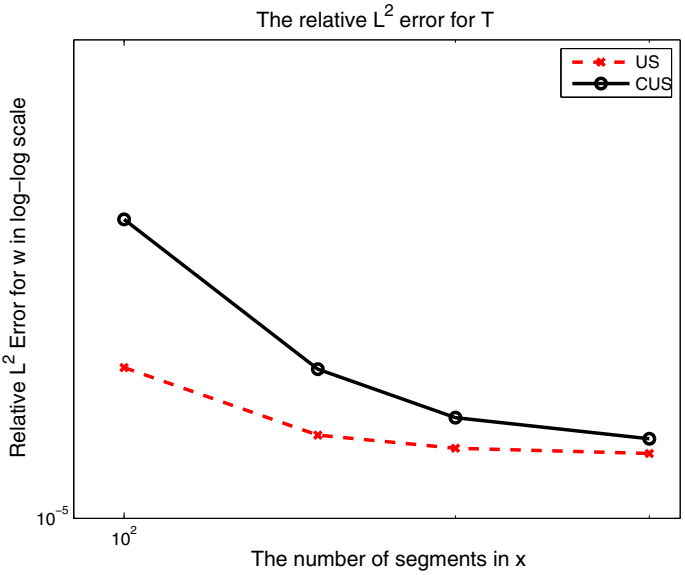

Fig. 9 Relative L^2 error for T with $p_B(x)$ of (4.3) at $t_* = 500$ and $\Delta t = 10$ in log–log scale. The convergence rates of the US and CUS methods are 0.1120 and 0.2753 respectively

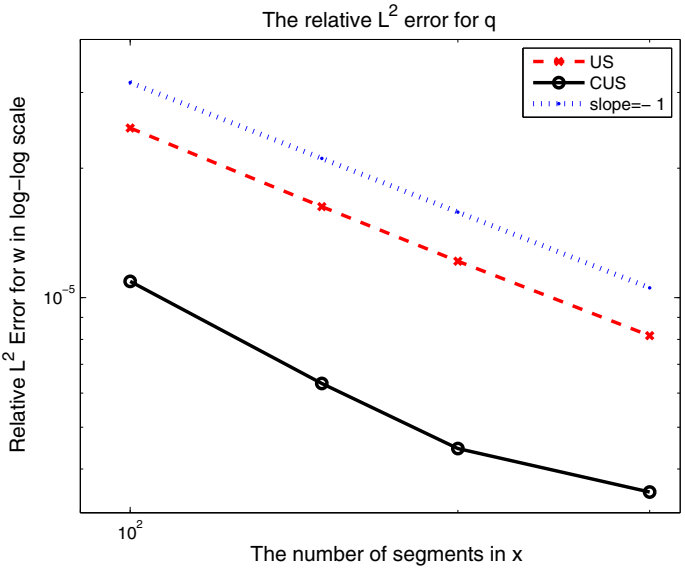

Fig. 10 Relative L^2 error for q with $p_B(x)$ of (4.3) at $t_* = 500$ and $\Delta t = 10$ in log–log scale. The convergence rates of the US and CUS methods are 1.0285 and 1.2906 respectively

Remark 4.1 If we drop the term **F** in (1.11), the CUS scheme converges with a rate of 2. However in the simulations of the physical model (1.5), since the term **F** consists of large quantities, the rate of convergence is <2.

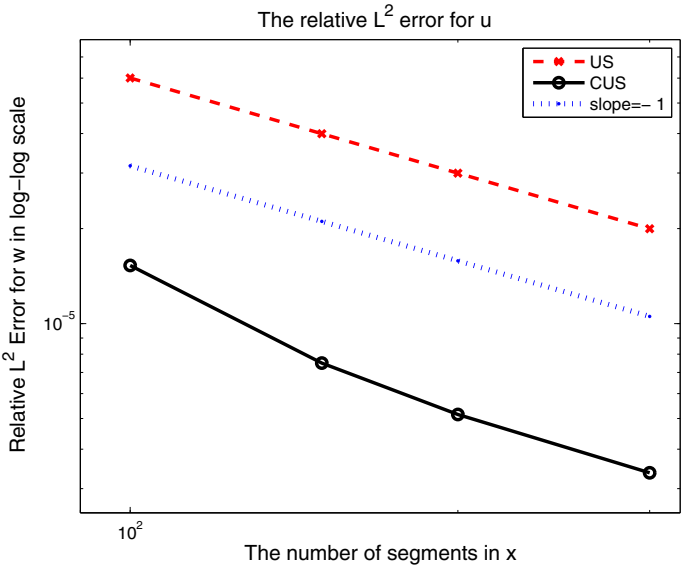

Fig. 11 Relative L^2 error for u with $p_B(x)$ of (4.3) at $t_* = 500$ and $\Delta t = 10$ in log–log scale. The convergence rates of the US and CUS methods are 1.0018 and 1.5688 respectively

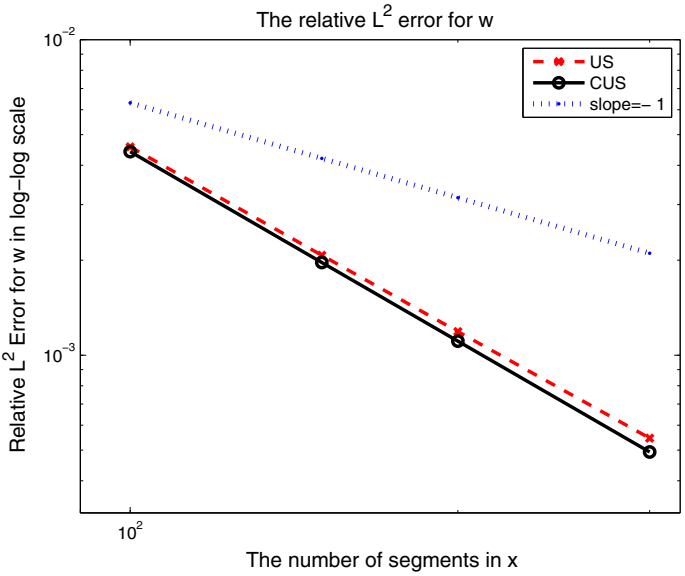

Fig. 12 Relative L^2 error for ω with $p_B(x)$ of (4.3) at $t_* = 500$ and $\Delta t = 10$ in log–log scale. The convergence rates of the US and CUS methods are 1.9464 and 1.9950 respectively

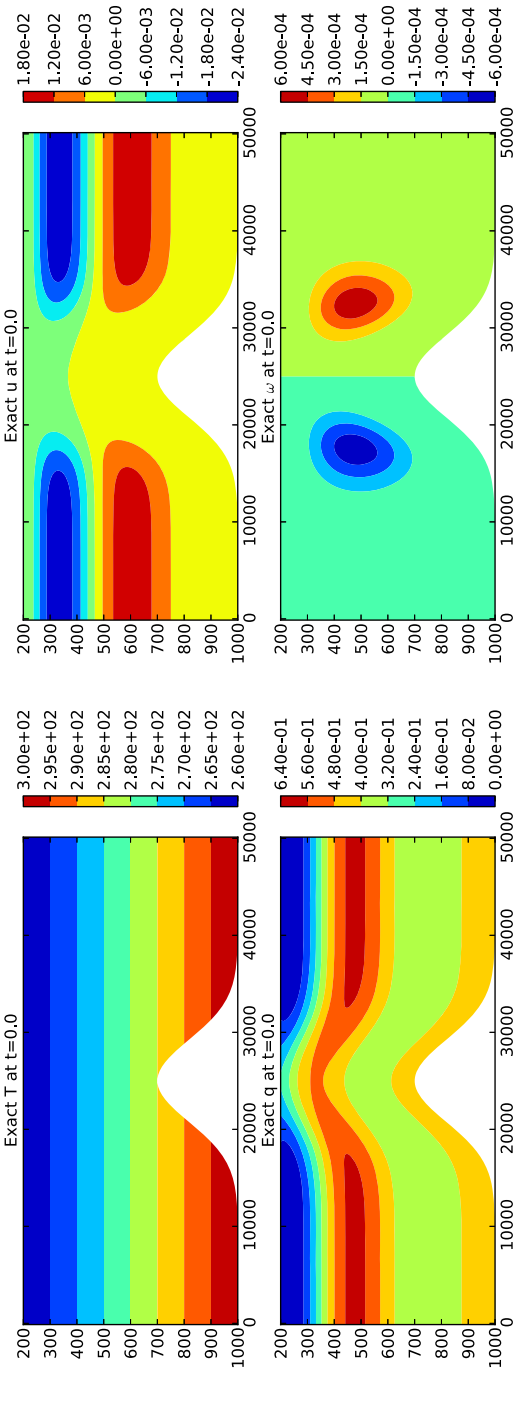

Fig. 13 Initial values of T, q, u, and ω with (4.4)

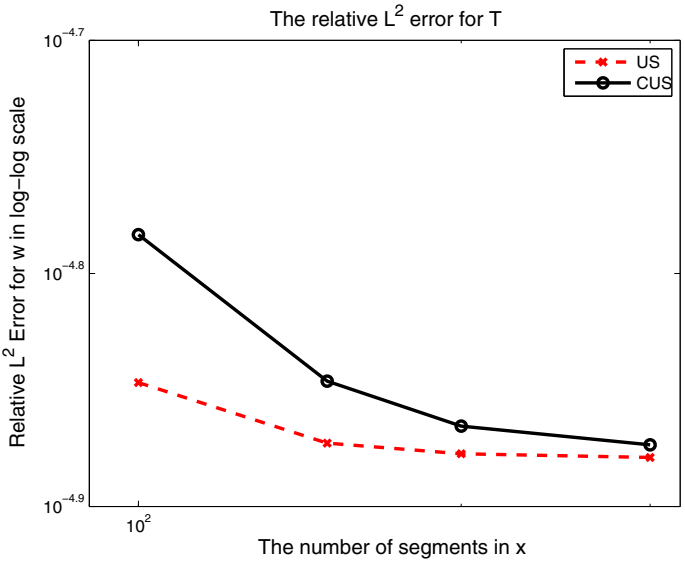

Fig. 14 Relative L^2 error for T with $p_B(x)$ of (4.4) at $t_* = 500$ and $\Delta t = 10$ in log–log scale. The convergence rates of the US and CUS methods are 0.1015 and 0.2728 respectively

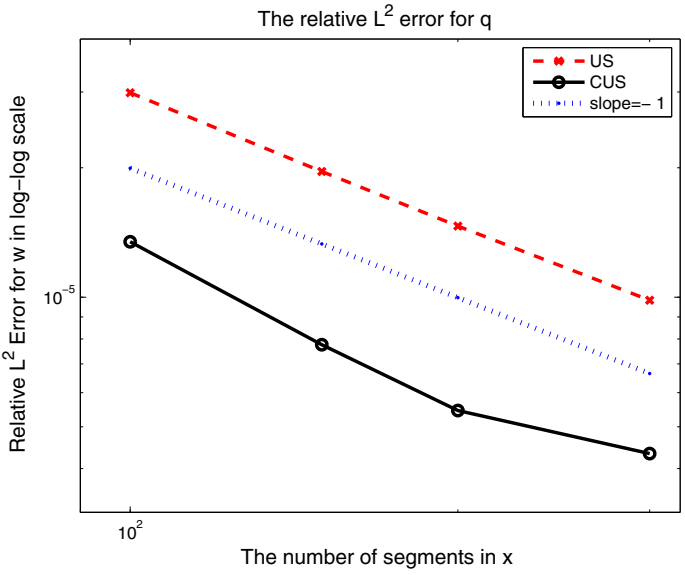

Fig. 15 Relative L^2 error for q with $p_B(x)$ of (4.4) at $t_* = 500$ and $\Delta t = 10$ in log–log scale. The convergence rates of the US and CUS methods are 1.0293 and 1.3030 respectively

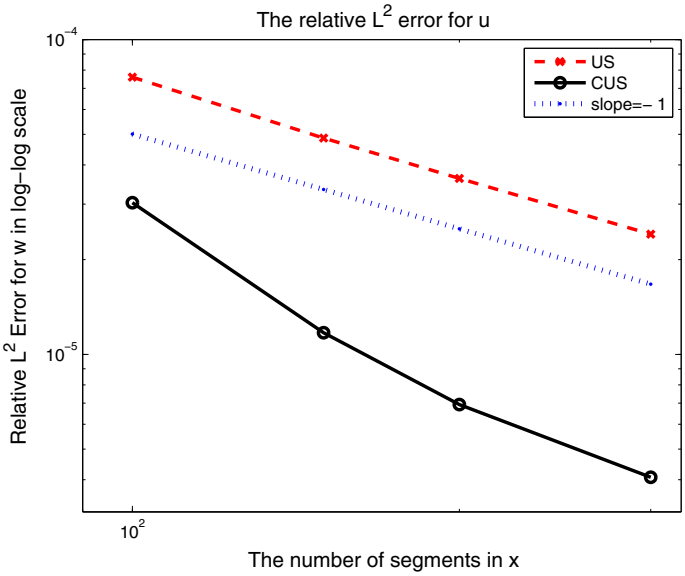

Fig. 16 Relative L^2 error for u with $p_B(x)$ of (4.4) at $t_* = 500$ and $\Delta t = 10$ in log–log scale. The convergence rates of the US and CUS methods are 1.067 and 2.1299 respectively

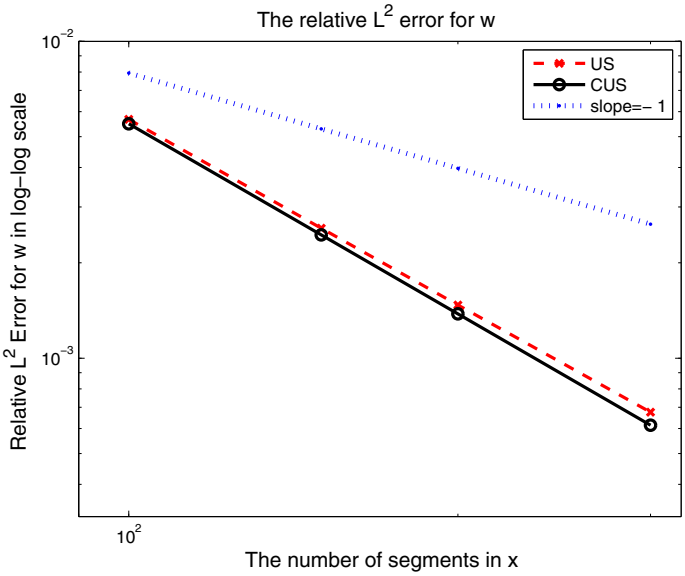

Fig. 17 Relative L^2 error for ω with $p_B(x)$ of (4.4) at $t_* = 500$ and $\Delta t = 10$ in log–log scale. The convergence rates of the US and CUS methods are 1.9461 and 1.9917 respectively

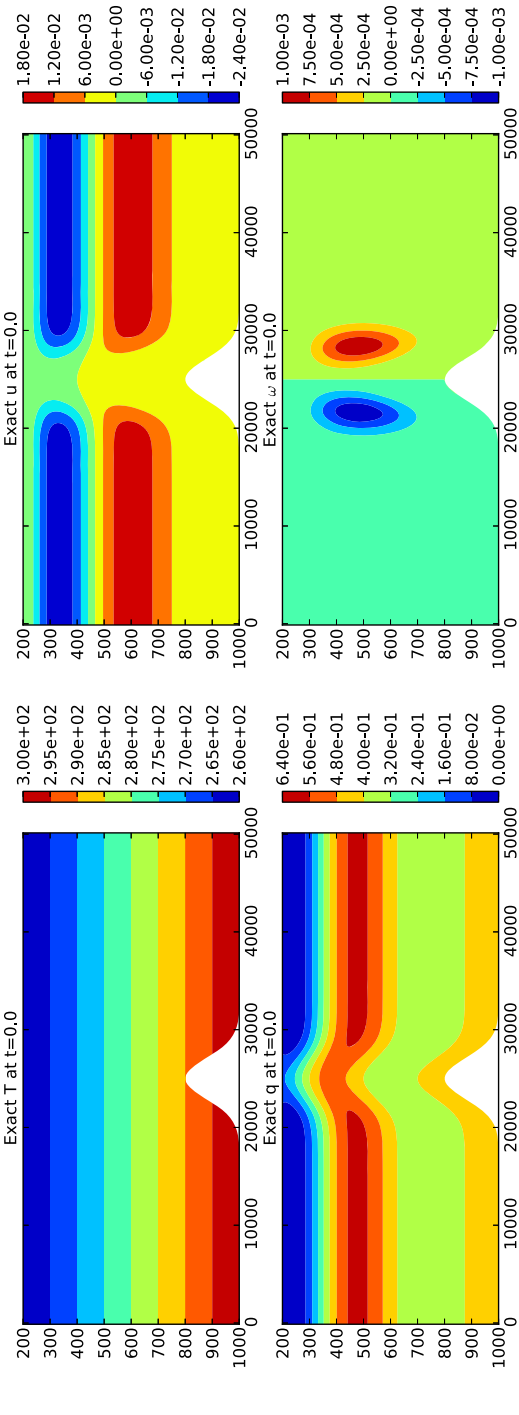

Fig. 18 Initial values of T, q, u, and ω with (4.5)

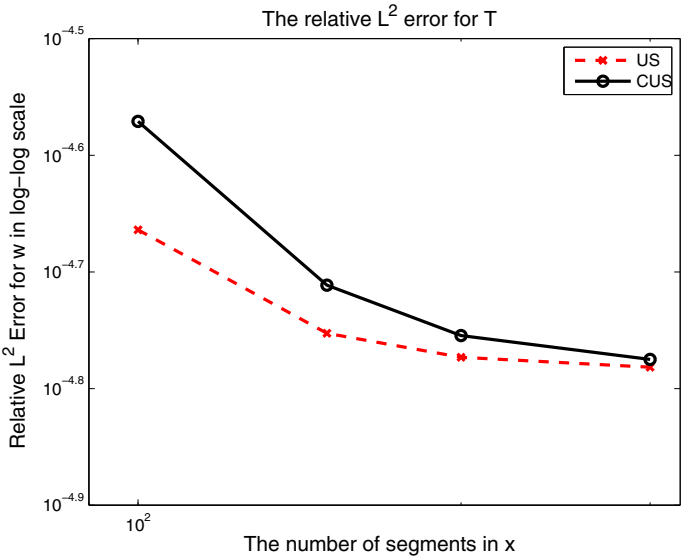

Fig. 19 Relative L^2 error for T with $p_B(x)$ of (4.5) at $t_* = 500$ and $\Delta t = 10$ in log–log scale. The convergence rates of the US and CUS methods are 0.3629 and 0.6100 respectively

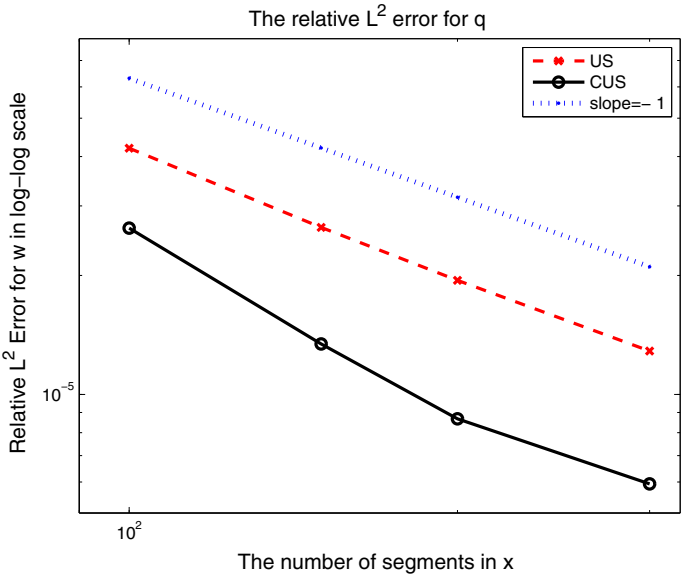

Fig. 20 Relative L^2 error for q with $p_B(x)$ of (4.5) at $t_* = 500$ and $\Delta t = 10$ in log–log scale. The convergence rates of the US and CUS methods are 1.1112 and 1.6025 respectively

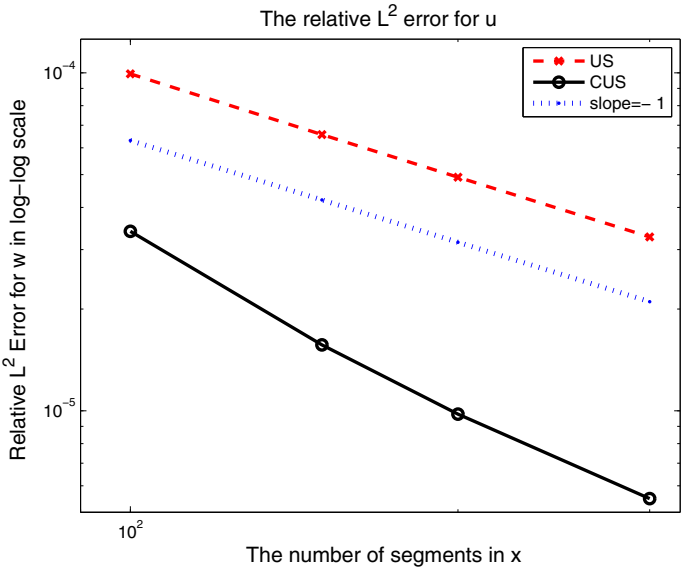

Fig. 21 Relative L^2 error for u with $p_B(x)$ of (4.5) at $t_* = 500$ and $\Delta t = 10$ in log–log scale. The convergence rates of the US and CUS methods are 1.0151 and 1.7980 respectively

4.1 Simulation 1: the case of a relatively flat topography

We set

$$p_B(x) = 1000 - 150 \exp\left(-\left(\frac{x - 25000}{6000}\right)^2\right). \tag{4.3}$$

Figure 8 shows the domain and the initial values of T, q, u, and ω. Figures 9, 10, 11, and 12 show the relative L^2 errors for T, q, u, and ω in log–log scale.

For q and u, the US scheme converges with a rate of 1, and the CUS scheme converges with a rate of 1.3 and 1.57 respectively. The convergence rate of ω is of order 2 using either the US or the CUS scheme because we apply identical methods for ω. Since we impose a physical restriction on T, see (1.4) and $(4.1)_1$, the convergence rate for T is as low as of order 0.1 for the US (or of order 0.3 for the CUS). However the relative L^2 error for T is less than 10^{-4}, which demonstrate a satisfactory accuracy of T.

4.2 Simulation 2: the case of a higher topography

We set

$$p_B(x) = 1000 - 300 \exp\left(-\left(\frac{x - 25000}{6000}\right)^2\right). \tag{4.4}$$

In this case the mountain determined by (4.4) is higher than (but as wide as) the one in Sect. 4.1. Figure 13 shows the domain and the initial values of T, q, u, and ω. Figures 14, 15, 16, and 17 show the relative L^2 errors for T, q, u, and ω, respectively, in log–log scale. We notice

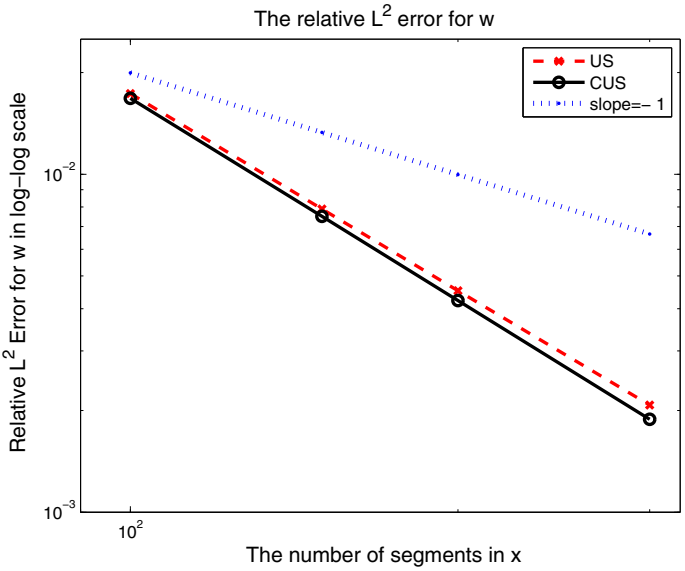

Fig. 22 Relative L^2 error for ω with $p_B(x)$ of (4.5) at $t_* = 500$ and $\Delta t = 10$ in log–log scale. The convergence rates of the US and CUS methods are 1.9390 and 1.9872 respectively

that the convergence rates for this case are compatible with those in Sect. 4.1. Therefore we see that our US (or CUS) scheme is flexible towards the height of the domain.

4.3 Simulation 3: the case of a narrow topography

In this simulation, we make the obstacle narrow by taking,

$$p_B(x) = 1000 - 200 \exp\left(-\left(\frac{x - 25000}{3000}\right)^2\right). \tag{4.5}$$

Figure 18 shows the domain and the initial values of T, q, u, and ω. Figures 19, 20, 21, and 22 show the relative L^2 errors for T, q, u, and ω, respectively, in log–log scale. We notice that the convergence rates for this case are compatible with those in Sect. 4.1.

Acknowledgments This work was supported in part by NSF Grants DMS 1206438 and DMS 1212141, and by the Research Fund of Indiana University. The authors would like to thank Professor Roger Temam and Dr. Joseph Tribbia for their suggestion and advice.

References

1. Gill, A.E.: Atmosphere-Ocean Dynamics. Academic Press, New York (1982)
2. Haltiner, G.J.: Numerical Weather Prediction. Wiley, New York (1971)
3. Rogers, R.R., Yau, M.K.: A Short Course in Cloud Physics, 3rd edn. Pergamon Press Oxford, New York (1989)

4. Oliger, Joseph, Sundström, Arne: Theoretical and practical aspects of some initial boundary value problems in fluid dynamics. SIAM J. Appl. Math. **35**(3), 419–446 (1978)
5. Temam, R., Tribbia, J.: Open boundary conditions for the primitive and Boussinesq equations. J. Atmos. Sci. **60**(21), 2647–2660 (2003)
6. Chen, Q.S., Laminie, J., Rousseau, A., Temam, R., Tribbia, J.: A 2.5D model for the equations of the ocean and the atmosphere. Anal. Appl. (Singap.) **5**(3), 199–229 (2007)
7. Chen, Q., Shiue, M.-C., Temam, R.: The barotropic mode for the primitive equations. J. Sci. Comput. **45**(1–3), 167–199 (2010)
8. Chen, Q., Temam, R., Tribbia, J.J.: Simulations of the 2.5D inviscid primitive equations in a limited domain. J. Comput. Phys. **227**(23), 9865–9884 (2008)
9. Rousseau, A., Temam, R., Tribbia, J.: Boundary conditions for the 2D linearized PEs of the ocean in the absence of viscosity. Discrete Contin. Dyn. Syst. **13**(5), 1257–1276 (2005)
10. Rousseau, A., Temam, R., Tribbia, J.: Numerical simulations of the inviscid primitive equations in a limited domain. In: Calgaro, C., Coulombel, J.-F., Goudon, T. (eds.) Analysis and Simulation of Fluid Dynamics, Advances in Mathematical Fluid Mechanics, pp. 163–181. Birkhäuser, Basel (2007)
11. Rousseau, A., Temam, R., Tribbia, J.: The 3D primitive equations in the absence of viscosity: boundary conditions and well-posedness in the linearized case. J. Math. Pures Appl. (9) **89**(3), 297–319 (2008)
12. Rousseau, A., Temam, R.M., Tribbia, J.J.: Boundary value problems for the inviscid primitive equations in limited domains. In: Handbook of Numerical Analysis, vol. XIV. Special Volume: Computational Methods for the Atmosphere and the Oceans, vol. 14 of Handbook of Numerical Analysis, pp. 481–575. Elsevier, North-Holland, Amsterdam (2009)
13. Chen, Q., Shiue, M.-C., Temam, R., Tribbia, J.: Numerical approximation of the inviscid 3D primitive equations in a limited domain. ESAIM Math. Model. Numer. Anal. **46**(3), 619–646 (2012)
14. Hong, Y., Temam, R., Bousquet, A., Tribbia, J.: Numerical weather prediction with primitive equations with humidity in two dimension using finite volume method (preprint)
15. Zelati, M.C., Temam, R.: The atmospheric equation of water vapor with saturation. Boll. Unione Mat. Ital. (9) **5**(2), 309–336 (2012)
16. Lions, J.-L., Temam, R., Wang, S.H.: New formulations of the primitive equations of atmosphere and applications. Nonlinearity **5**(2), 237–288 (1992)
17. Petcu, M., Temam, R.M., Ziane, M.: Some mathematical problems in geophysical fluid dynamics. In: Handbook of Numerical Analysis, vol. XIV. Special Volume: Computational Methods for the Atmosphere and the Oceans, vol. 14 of Handbook of Numerical Analysis, pp. 577–750. Elsevier, North-Holland, Amsterdam (2009)
18. LeVeque, R.J.: Finite Volume Methods for Hyperbolic Problems. Cambridge Texts in Applied Mathematics. Cambridge University Press, Cambridge (2002)
19. Versteeg, H.K., Malalasekera, W.: An Introduction to Computational Fluid Dynamics: The Finite Volume Method. Pearson Education Limited, London (2007)
20. Adamy, K., Bousquet, A., Faure, S., Laminie, J., Temam, R.: A multilevel method for finite volume discretization of the two-dimensional nonlinear shallow-water equations. Ocean Model. **33**(3–4), 235–256 (2010)
21. Kurganov, A., Levy, D.: Central-upwind schemes for the Saint-Venant system. M2AN Math. Model. Numer. Anal. **36**(3), 397–425 (2002)
22. Kurganov, A., Noelle, S., Petrova, G.: Semidiscrete central-upwind schemes for hyperbolic conservation laws and Hamilton–Jacobi equations. SIAM J. Sci. Comput. **23**(3), 707–740 (2001). (electronic)
23. Kurganov, A., Petrova, G.: Central-upwind schemes for two-layer shallow water equations. SIAM J. Sci. Comput. **31**(3), 1742–1773 (2009)
24. Kurganov, A., Petrova, G., Popov, B.: Adaptive semidiscrete central-upwind schemes for nonconvex hyperbolic conservation laws. SIAM J. Sci. Comput. **29**(6), 2381–2401 (2007)
25. Kurganov, A., Tadmor, E.: New high-resolution central schemes for nonlinear conservation laws and convection–diffusion equations. J. Comput. Phys. **160**(1), 241–282 (2000)
26. Nessyahu, H., Tadmor, E.: Nonoscillatory central differencing for hyperbolic conservation laws. J. Comput. Phys. **87**(2), 408–463 (1990)
27. Calhoun, D., LeVeque, R.J.: A Cartesian grid finite-volume method for the advection-diffusion equation in irregular geometries. J. Comput. Phys. **157**(1), 143–180 (2000)
28. LeVeque, R.J.: Cartesian grids and rotated difference methods for multi-dimensional flow. In: Proceedings of International Conference on Scientific Computation (Hangzhou, 1991), vol. 1 of Series Applied Mathematics, pp. 76–85. World Scientific Publishing, River Edge, NJ (1992)

29. LeVeque, R.J., Calhoun, D.: Cartesian grid methods for fluid flow in complex geometries. In: Fauci, L.J., Gueron, S. (eds.) Computational modeling in biological fluid dynamics (Minneapolis, MN, 1999), vol. 124, pp. 117–143. IMA Volumes in Mathematics and its Applications, Springer, New York (2001)
30. Huang, W., Kappen, A.M.: A study of cell-center finite volume methods for diffusion equations. Electronic (1998)
31. Gie, G.-M., Temam, R.: Cell centered finite volume methods using Taylor series expansion scheme without fictitious domains. Int. J. Numer. Anal. Model. **7**(1), 1–29 (2010)
32. Gie, G.-M., Temam, R.: Convergence of the cell-centered Finite Volume discretization method (submitted) NULL